Solid State Sciences 174 (2026) 108204

Contents lists available at ScienceDirect

Solid State Sciences

journal homepage: www.elsevier.com/locate/ssscie

Machine learning interatomic potentials for NaPSO glasses: the critical role of training data

Marco Bertani *, Alfonso Pedone

Department of Chemical and Geological Sciences, University of Modena and Reggio Emilia, Italy

ARTICLE INFO

Keywords:
Amorphous electrolytes
All-solid-state sodium batteries
Machine learning interatomic potentials
Molecular dynamics
Database
DFT functional

ABSTRACT

The performance of five machine learning interatomic potentials (MLIPs), based on MACE, DeePMD, and GRACE-FS architectures, is assessed in reproducing the structural and mechanical properties of $Na_4P_2S_{7-x}O_x$ mixed oxy-thiophosphate glasses, promising candidates for next-generation all-solid-state sodium batteries. The glass series ($0 \leq x \leq 3.5$) was chosen to explore the effect of oxygen incorporation on short- and medium-range structural order (SRO and MRO), a particularly challenging task as experimental data show non-linear trends in density, conductivity, and structural units with composition. Universal MLIPs, trained on generic databases (MP0, MATPES-r2SCAN, METPES-PBE) or on datasets comprising only the elements relevant to glassy solid electrolytes (GRACE-GSE), provide stable molecular dynamics but often predict artifacts such as edge-sharing tetrahedra or P–P chains, and fail to reproduce the SRO evolution. A DeePMD MLIP, trained via concurrent learning on crystalline Na–P–S–O structures without stoichiometry-specific data, exhibits similar limitations. Among the universal MLIPs, MATPES-r2SCAN reproduces density, mechanical properties, and anion (S and O) speciation with reasonable accuracy. Fine-tuning MP0 on the specific glass compositions (FT-MP0) significantly improves structural reproduction, accurately capturing density trends, mechanical properties, and the preference of oxygen for bridging positions. Nonetheless, even FT-MP0 cannot accurately reproduce the disproportionation reaction of dimeric P^1 units converting to isolated P^0 units and P^2 chains associated with oxygen incorporation. These results highlight that universal MLIPs are valuable starting points for approximate simulations or database generation, but fine-tuning on both composition and relevant structural features is essential to accurately reproduce the short- and medium-range order of NaPSO glasses.

1. Introduction

The battery market is currently dominated by lithium-ion batteries (LIBs) utilizing liquid organic electrolytes. However, the high cost and scarsity of the raw materials [1], along with environmental and social impact [2–5], and safety concerns [6,7] are pushing the scientific community to explore alternatives beyond lithium-based technologies. Among these, all-solid-state-sodium-batteries (ASSSBs) [8] have emerged as promising candidates for grid-scale energy storage [9], owing to the abundance and more sustainable extraction of sodium. This not only reduces social and environmental burdens compared to LIBs but also enhances safety while maintaining comparable energy density. Realizing ASSSBs in practical applications requires the development of new solid-state electrolytes (SSEs), that are both highly conductive and chemically/electrochemically stable [10–12]. Ideal SSEs should exhibit high Na^+ conductivity ($>10^{-4}$ S/cm) at room temperature, be stable across a wide electrochemical window(~0–4 V versus Na/Na^+), and be processable into a fully dense and monolithic sheet to suppress dendrite growth [13–16].

Among SSEs, glassy solid electrolytes (GSEs) are particularly attractive due to their tunable composition, ease of processing, and superior chemical stability compared to crystalline counterparts [17]. In recent years, sodium thiophosphate (NaPS) glasses have gained increasing attention as valuable materials for ASSSBs as they show higher ionic conductivity [18–22] ($>10^{-2}$ S/cm) with respect to oxide glasses (max $\sim 10^{-6}$ S/cm) and lower melting temperatures, which enable cost-effective synthesis. However, their poor electrochemical stability, sensitivity to atmospheric conditions limit their direct application. To address these limitations, mixed oxy-thiophosphate (NaPSO) glasses have been proposed [23–27] aiming to retain the high ionic

This article is part of a special issue entitled: Computational modelling of materials published in Solid State Sciences.

* Corresponding author.
E-mail address: marco.bertani@unimore.it (M. Bertani).

https://doi.org/10.1016/j.solidstatesciences.2025.108204
Received 13 October 2025; Received in revised form 22 December 2025; Accepted 30 December 2025
Available online 3 January 2026
1293-2558/© 2026 The Authors. Published by Elsevier Masson SAS. This is an open access article under the CC BY license (http://creativecommons.org/licenses/by/4.0/).

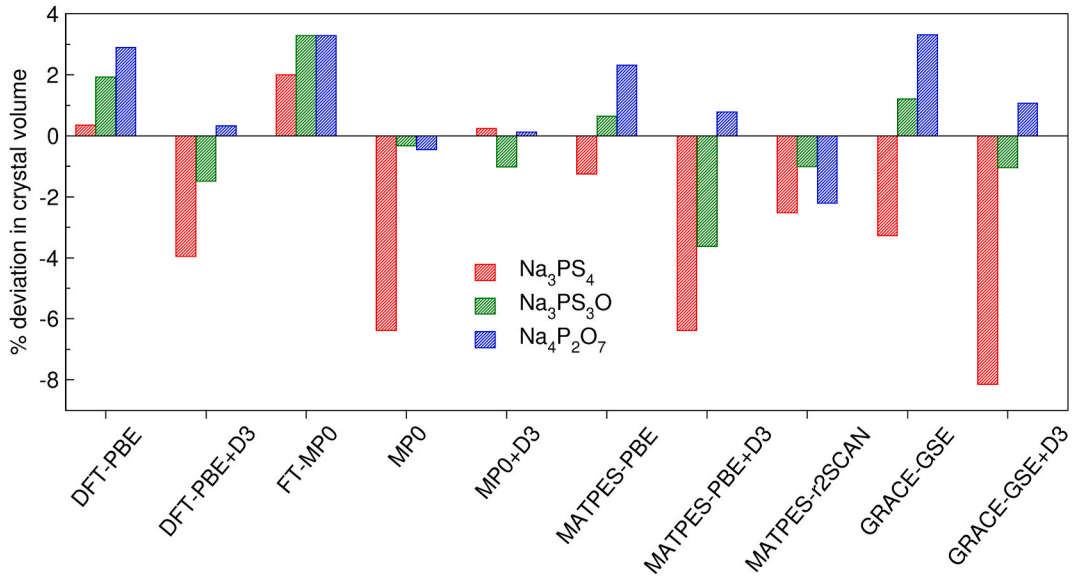

Fig. 3. Percentage deviation between experimental and simulated crystal volume for Na3PS4, Na3PS3O, and Na4P2O7 crystals. Negative values indicate a contraction of the crystalline volume while positive ones indicate an expansion.

They also show that for pure sulfide crystal (Na_3PS_4), PBE functional and MLIPs trained on it give good agreement with experimental density, while the addition of the D3 dispersion correction leads to overestimate it. The opposite trend is observed for pure oxide phosphate crystal ($Na_4P_2O_7$), while mixed oxy-sulfide (Na_3PS_3O) gives intermediate behavior. This demonstrates that the overestimation observed in the glass simulations can originate from the excessive strength of the D3 correction in these P–S–O systems.

In this context, it is also insightful to evaluate the behavior of the MATPES-r2SCAN potential relative to MATPES-PBE and to the underlying DFT functionals. Although r2SCAN does not contain an explicit long-range dispersion term, its enhanced treatment of intermediate-range correlation often leads to improved equilibrium geometries compared to PBE. Our crystalline benchmarks reflect this trend: for the sulfide Na_3PS_4, both MATPES potentials underestimate the experimental volume, but r2SCAN yields a slightly larger contraction. Conversely, for the oxide-rich structures (Na_3PS_3O and $Na_4P_2O_7$), MATPES-PBE systematically overestimates the volume, whereas MATPES-r2SCAN gives a modest underestimation, closer to experiment. This inversion in behavior is consistent with large-scale benchmarks reporting that r2SCAN corrects much of PBE's overexpansion while providing cell volumes comparable in accuracy to SCAN and PBEsol [69,70]. Importantly, because r2SCAN lacks a non-local dispersion kernel, its performance remains reliable for ionic and covalent solids such as those studied here, while dispersion-dominated systems (layered and molecular crystals) would still require corrections like rVV10 or D4 [71,72]. Taken together, these observations reinforce that the differences between MATPES-PBE and MATPES-r2SCAN arise from their distinct treatments of correlation rather than from dispersion effects, and that r2SCAN behaves consistently with its broader performance across solid-state materials.

3.2. Elastic modules

Solid electrolytes must withstand severe mechanical stresses during battery charge and discharge while ensuring optimal interfacial contact with the electrodes. Moreover, the elastic properties are directly related to the curvature around the minimum of the potential energy surface. Therefore, an accurate description of the elastic properties is a prerequisite for a reliable interatomic potential for these systems. The structure of inverted glasses, which have more modifiers than glass formers such as the ones studied here, is mainly made of anionic SRO bound by ionic forces [73,74]. Consequently, the elastic properties are largely determined by the ionic non-bridging anions (NBS and NBO) rather than by covalent bridging units (BS and BO). This effect is particularly pronounced in sulfur-rich glasses, as sulfur forms weaker covalent and ionic bonds compared to oxygen.

The Young's and bulk modules, which describe the material's response to uniaxial stress and hydrostatic compression, respectively, were computed using all the considered MLIPs and compared with experimental results [26] in panels (b) and (c) of Fig. S1 of the ESI while MAEs value are showed in Fig. 2.

The Young's and bulk moduli increase with the substitution of sulfur by oxygen, a trend generally captured by all MLIPs. The finetuned FT-MP0 model yields the best agreement for the Young's modulus and good results for the Bulk one, with a MAE of 1.6 GPa and 2.2 GPa, respectively—a substantial improvement over the pretrained MP0, which underestimates it (MAE = 11.4 GPa and 7.5 GPa in the same order). The UMLIPs trained on the MATPES databases show that r2SCAN generally predicts higher and better modules with respect to PBE, even if it still underestimates the experimental values (MATPES-r2SCAN: MAE = 2.8 GPa and 3.2 GPa for Young's and bulk moduli, respectively; MATPES-PBE: MAE = 5.6 GPa and 5.7 GPa for Young's and bulk moduli, respectively). DeePMD gives the best agreement for the bulk modulus (MAE = 1.6 GPa) but underestimates the Young's modulus by 3.5 GPa on average. The GRACE-GSE MLIP reproduces the Young's modulus reasonably well (MAE = 1.7 GPa), although with large error bars (±1.0–3.5 GPa). However, it performs poorly for the bulk modulus, strongly overestimating experimental values (MAE = 5.3 GPa). It is also worth noting that the seemingly good agreement for the elastic properties likely arises from systematic overestimation of density, rather than from the accurate description of the underlying structural features and bond forces.

Overall, the UMLIPs reproduce the density and elastic properties with reasonable accuracy, with MATPES-r2SCAN giving the best results among them. However, their performance is still not sufficient to consider these models fully reliable for quantitative predictions. In contrast, the fine-tuned FT-MP0 potential shows a clear improvement, particularly in capturing the Young's modulus and density trends. This highlights that, although UMLIPs are valuable as transferable starting points, fine-tuning or dedicated training on system-specific datasets remains essential to achieve quantitative agreement with experiments.

3.3. Structural analysis

The structure of $Na_4P_2S_{7-x}O_x$ glasses has been experimentally investigated using NMR, IR, and RAMAN techniques [23]. In all the glass series, phosphorus was found to be four-coordinated, forming different structural units depending on the connectivity with neighboring phosphorus atoms. Specifically, P^0, P^1, and P^2 SRO are present, corresponding to tetrahedra with 0, 1, and 2 bridging atoms (S or O). In addition, a sulfur-deficient unit has been identified, in which two phosphorus atoms are linked through a homonuclear bond and each is further bonded to three sulfur atoms (P^{1P}). To provide a clearer picture of these motifs, Fig. 4 shows representative structures extracted from the MP0 MD simulations, illustrating the characteristic structural units identified in these glasses.

Ab-initio and ML simulations of $Na_4P_2S_7$ glass [22,75], also predict the occurrence of three coordinated phosphorus (P^3), edge-sharing tetrahedra (P^{2ES}), and multiple P-P bonds involving up to four atoms (P-P chains), which have not been observed experimentally. A graphical representation of sulfur-deficient and P-P chains SRO can be found in Fig. 5.

The presence of sulfur-deficient units, such as P^{1P} and $P^{3:}$ (Fig. 5a and b), implies the formation of free sulfur in the glass, which may generate S-S bonds and sulfur chains that hinder Na diffusion. The coordination of sodium has not been experimentally determined for these glasses; however, values between 6 and 8 have been reported in related crystalline phases [76].

3.3.1. Phosphorous

All the MLIPs predict predominantly four-coordinated phosphorus, although a small fraction of three-coordinated species is always present. The FT-MP0, MATPES-r2SCAN, MATPES-PBE, and DeePMD potentials yield a relatively high amount of $P^{3:}$ units (6–8 %) in the pure sulfide glass, which decreases to 2–3 % for the three MACE models and ~4 % for DeePMD. In contrast, GRACE-GSE and MP0 predict nearly constant fraction of $P^{3:}$, around 3.5 % and 2.5 %, respectively. The occurrence of this species can be attributed to the high quench rate employed in the simulations. To test this hypothesis, we performed simulations with the FT-MP0 potential at a quench rate of 0.5 K/ps, i.e., ten times slower. Under these conditions, the fraction of $P^{3:}$ dropped to ~0.5 % across all glasses, while other structural features remained essentially unaffected.

The fraction of structural units was experimentally determined from ^{31}P NMR [23]. It was found that pure sulfide glass is dominated by P^1 species that disproportionate to P^0 and P^2 when oxygen is added. The percentages of SROs obtained experimentally and from simulations are reported in Fig. 6, as well as the percentage of P^{1P} units.

Fig. 6 shows that none of the tested potentials can reproduce the experimental amount of P^n species and that the improvement of the finetuning for this property is significant but not sufficient to have a good description of the SRO trends. FT-MP0 (panel a) gives the best agreement for the pure sulfide glass, and shows a slightly decreasing trend for P^1 together with an increasing trend for P^2 and P^0 (except for the initial oxygen addition from 0 to 0.5) but stays far from a good reproduction of the disproportionation reaction occurring when oxygen substitutes for sulfur. This highlights both the importance of training on system-specific data and the need for improvement of the database. In particular, including in the training set more polymerized glasses—characterized by higher P^2 contents and a greater number of bridging units—would likely improve the agreement with experiment. The P^{1P} amount is slightly underestimated, although it follows the correct decreasing trend. The three MACE foundation models (MP0, panel c, MATPES-r2SCAN, panel d, and MATPES-PBE, panel e) yield similar results, with nearly 40–50 % of P^0 and P^1 in pure sulfide glass. MP0 reproduces the correct decreasing trend of P^{1P}, whereas the two MATPES potentials predict a negligible amount of this unit. Upon oxygen substitution for sulfur, both P^1 and P^2 fractions increase while P^0 decreases, in contrast with experiment, demonstrating the limited reliability of these UMLIPs in reproducing the short-to medium-range structural features of these GSEs. Similar considerations apply to the DeePMD potential which predicts an initial structure (at zero oxygen content) composed of nearly equal amounts of P^0, P^1, and P^2 with no P^{1P}. As oxygen content increases, the P^1 fraction rises at the expense of P^2, while P^0 remains constant. GRACE-GSE, instead, predicts the pure sulfide glass to consist of ~60 % of P^1, ~30 % P^0, and ~10 % P^2. While this is qualitatively consistent with experiment—although experimental data indicate higher P^1 and lower P^0 and P^2—no clear compositional trend is observed upon oxygen addition, with values oscillating around the same values. For the FT-MP0 potential, we also analyzed the P^n speciation in the liquidus phase (1800 K) and its evolution during quenching for glasses with x = 0 and x = 3.5, as reported in Fig. S2 of the ESI. The oxygen-free glass (x = 0) exhibits a highly depolymerized structure at high temperature, characterized by a large fraction of P^0 species (~80 %) and a smaller fraction of P^1 (~20 %). During quenching, the amount of P^0 decreases, while P^1 and P^2 progressively increase, eventually reaching the room-temperature distribution shown in Fig. 6. The glass with 50 % oxygen substitution (x = 3.5) starts from a markedly different speciation, with P^0 and P^1 both around ~45 % and P^2 at ~10

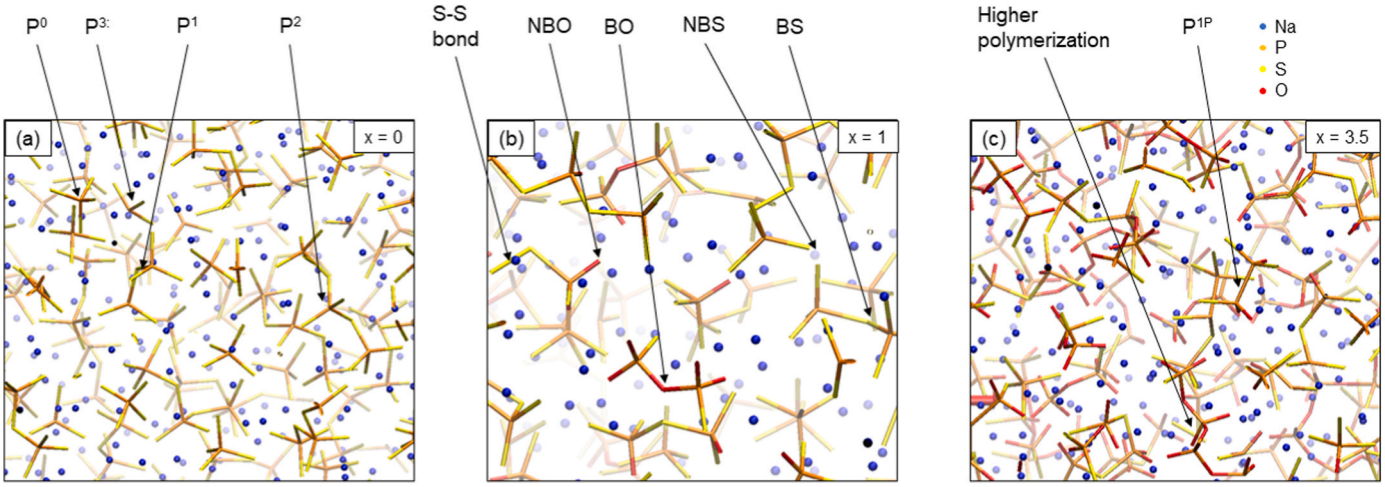

Fig. 4. Structures extracted from the 300K MD using MP0 MLIP of $Na_4P_2S_{7-x}O_x$ with x = 0 (panel a), x = 1 (panel b), and x = 3.5 (panel c). Na, P, S, and O atoms are represented as blue dots, orange, yellow, and red sticks, respectively. The SRO are highlighted to facilitate the visualization. (For interpretation of the references to colour in this figure legend, the reader is referred to the Web version of this article.)

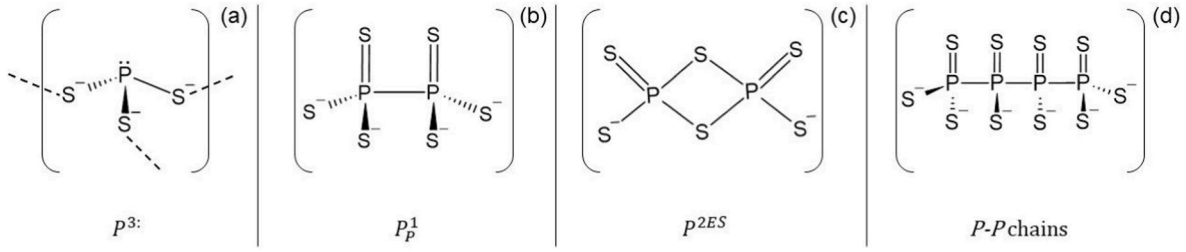

Fig. 5. Graphical representation of $P^{3:}$ (a), P^{1P} (b), P^{2ES} (c), and P-P chains SRO units.

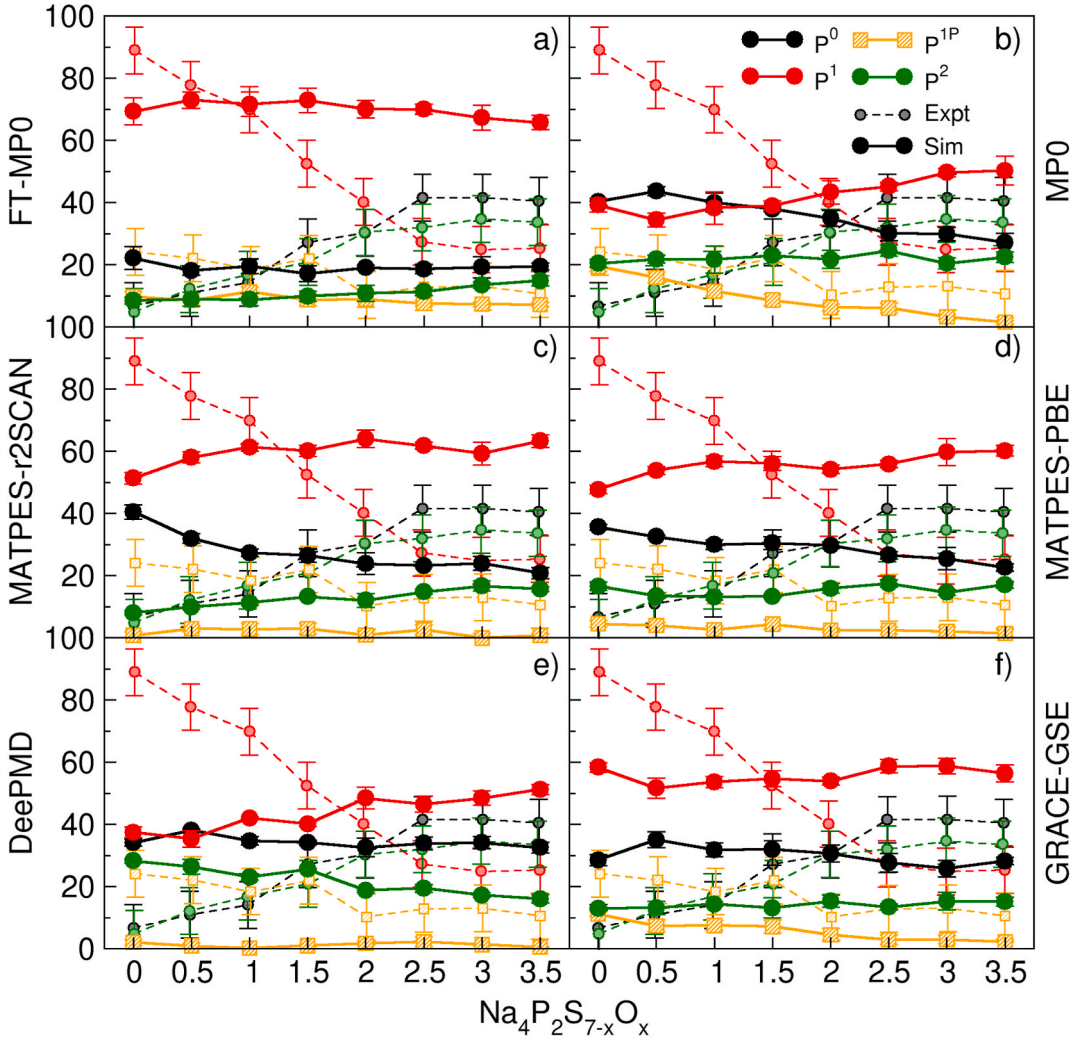

Fig. 6. Percentage of P^0, P^1, P^2, and P^{1P} structural units obtaind from MD simulations with FT-MP0 (a), MP0 (b), MATPES-r2SCAN (c), MATPES-PBE (d), DeePMD (e), and GRACE-GSE (f) MLIPs. Dashed lines represent experimental values [23]. It should be noted that P^1 units also include P^{1P}.

%. Although the qualitative trends during quenching resemble those of the oxygen-free composition, the changes are significantly less pronounced. These observations suggest that reducing the quench rate to values well below those explored here (0.5–5.0 K/ps) would likely improve the structural description of glasses with low oxygen content, while potentially worsening that of compositions with higher oxide character. This is probably due to an excessively polymerized representation of the liquidus state in the latter case.

The overall structures for the glasses with x = 0 and 3.5 generated with the different UMLIPs is reported in Fig. 7. At a first sight, we can observe that FT-MP0 model is the only one not reproducing evident artifacts such as P-P chains and edge sharing tetrahedra.

In MP0, MATPES-r2SCAN, and GRACE-GSE simulations of the pure sulfide $Na_4P_2S_7$ glass, we observed multiple P–P bonds forming chains of up to four phosphorus atoms (Fig. 5d), which have not been observed experimentally or in ab initio MD simulations.

A not negligible amount of P^{2SE} edge-sharing units (Fig. 5c) -not been observed experimentally-is predicted by the MP0, MATPES-PBE, and DeePMD potentials. In particular, MP0 predicts that 6–9 % of phosphorus atoms are involved in P^{2SE} units, with no clear dependence on the composition, while MATPES-PBE and DeePMD yield a decreasing trend from ~5.5 % to ~0.5 % and from ~10 % to ~3.5 %, respectively. In contrast, FT-MP0, MATPES-r2SCAN, and GRACE-GSE consistently predict less than 1 % of phosphorus atoms in P^{2SE} units across the entire

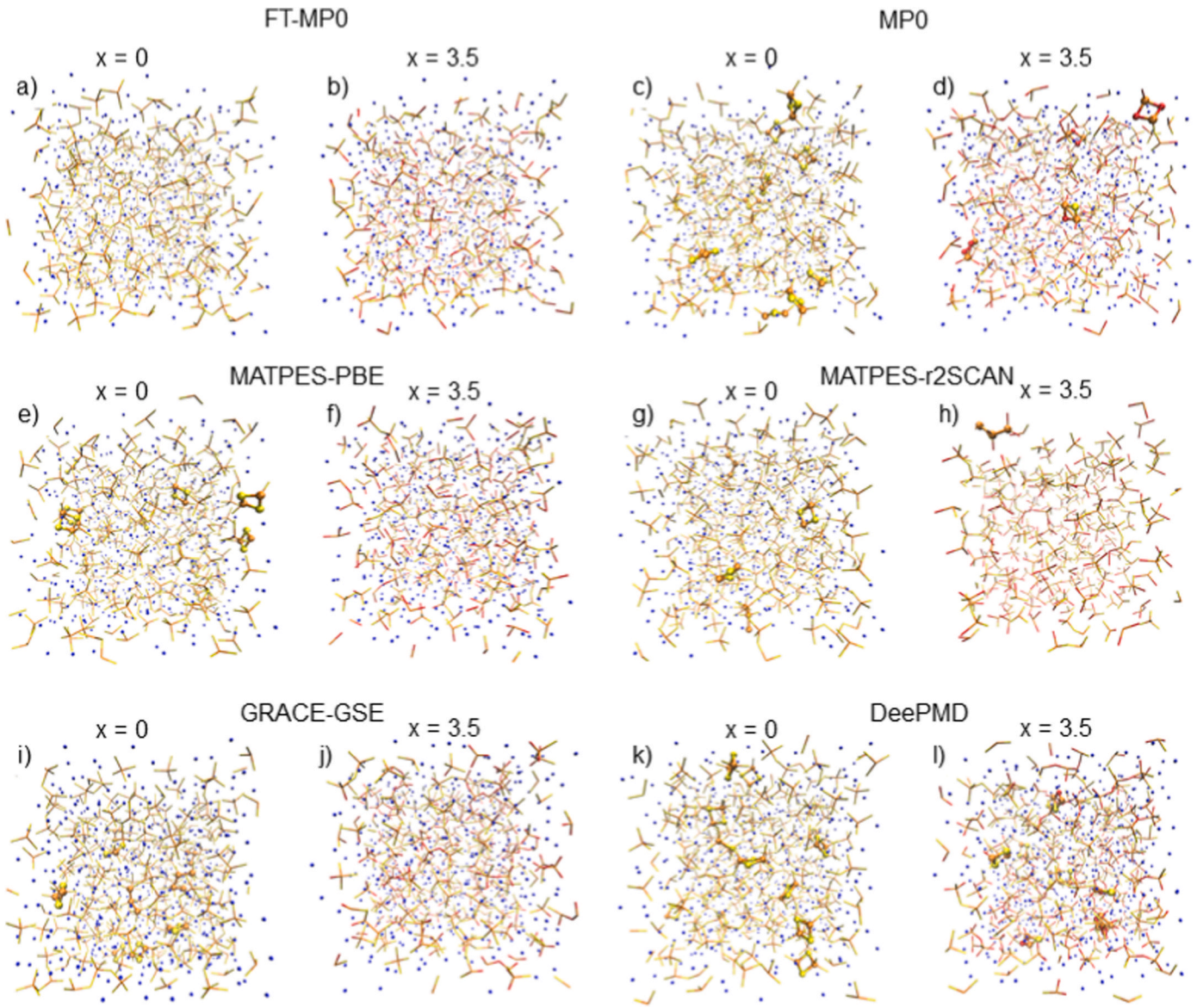

Fig. 7. Final structures of glasses x = 0 and x = 3.5 simulated with FT-MP0 (a, b), MP0 (c, d), MATPES-PBE (e, f), MATPES-r2SCAN (g, h), GRACE-GSE (i, j), and DeePMD (k, l). Artifacts such as P^{2S} or multiple P-P bonds are highlighted in the structures.

glass series. The presence of such structural artifacts is problematic since strongly impact the computed glass properties and highlights the need for careful validation and refinement of UMLIPs.

3.3.2. *Sulfur and oxygen*

The presence of sulfur-deficient units releases free sulfur, which tends to form S-S chains. All MLIPs predict a nearly constant fraction of sulfur atoms in such bonds, though with notable differences across models, as reported in Table S3 of the ESI. FT-MP0, GRACE-GSE, and MP0 give values in 2–4 % range, MATPES-PBE predicts a gradual increase from 1.7 % to 3.2 %, MATPES-r2SCAN gives 1.5–2.5 %, and DeePMD yields the lowest values, below 2 %. Across all potentials, most sulfur chains are dimers, but MP0, MATPES-PBE, and FT-MP0 also predict longer chains with average length of 2.0–2.3 and 4–21 % of three-membered chains. These predictions can be benchmarked against ab initio MD simulations of $Na_4P_2S_7$ glass, which reported 13.4 % of sulfur atoms in chains with an average length of 2.14. [22]. The same study also showed a temperature dependence, with more S-S chains at high T, and suggested that slower quenching suppresses homonuclear bonding. Our FT-MP0 simulations at a reduced cooling rate (0.5 K/ps) confirms this: the fraction of sulfur atoms chains decreases below 2 %, from 1.9 % in the pure sulfide to 0.5 % at 50 % of substitution.

We also analyzed the fractions of bridging (BS, BO) and non-bridging (NBS, NBO) anions, which can be experimentally determined from the distributions of structural units [23]. Fig. 8 reports the fractions of BS, BO, NBS, and NBO obtained from simulations as well as the experimental values [23].

Experimentally, the pure sulfide glass contains mostly NBS atoms, with a small fraction of BS atoms connecting P^1 units. Upon oxygen substitution, the fraction of NBS and BS decreases, while NBO and BO increase. For homogenous substitution, the crossing points of NBS/NBO and BS/BO fractions would occur at x = 3.5, but experiments show that oxygen preferentially occupies bridging sites due to its higher field strength, causing BS and BO to cross already at x = 2 [27]. The MLIPs qualitatively reproduce these substitution trends, but their fidelity varies. FT-MP0, MATPES-r2SCAN, and MATPES-PBE correctly capture oxygen's preference for bridging sites, with BS and BO converging around x = 2.5–3. In contrast, DeePMD, GRACE-GSE, and MP0 predict more random distributions, with MP0 even giving inverted NBO/NBS fractions at x = 3.5. This underscores the significant improvement achieved

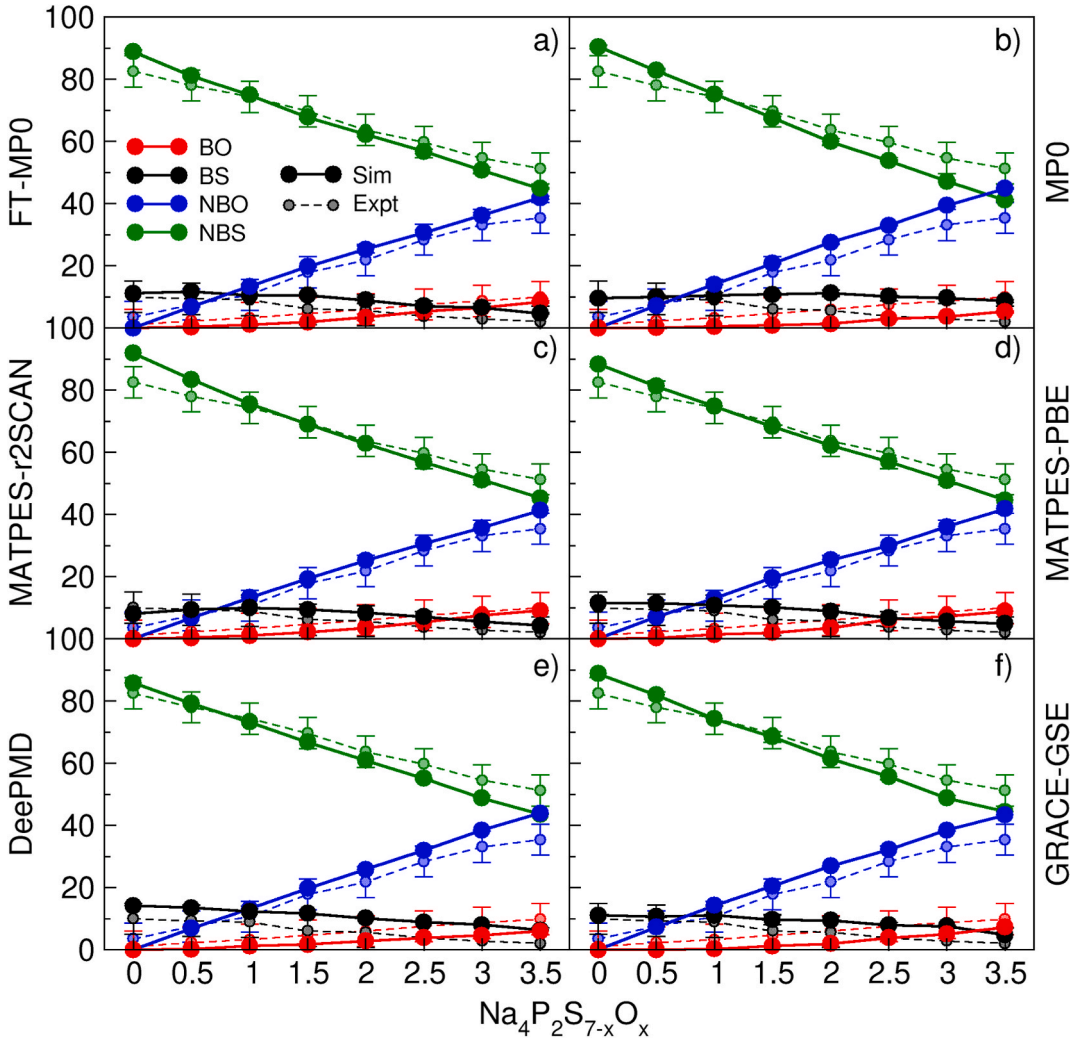

Fig. 8. Percentage of BO, BS, NBO, and NBS in the glass series obtaind from MD simulations with FT-MP0 (a), MP0 (b), MATPES-r2SCAN (c), MATPES-PBE (d), DeePMD (e), and GRACE-GSE (f) MLIPs. Dashed lines represent experimental values [23].

through fine-tuning (FT-MP0) and the value of high-quality datasets MATPES compared to MPRelax.

Taken together, the results highlight an important distinction: while FT-MP0 and the MATPES-based UMLIPs reproduce the oxygen and sulfur speciation across the glass series, they still fail to capture the short-range disproportionation reaction 2 $P^1 \rightarrow P^0 + P^2$ upon oxygen substitution. This point to a limitation of current UMLIPs. The structural environments contained in their training databases are sufficient to enforce correct speciation trends but insufficient to reproduce more subtle network rearrangements.

3.3.3. Sodium

Fig. 9 reports the Na-(S + O) coordination numbers of the $Na_4P_2S_{7-x}O_x$ glasses obtained with the different MLIPs. All models predict average sodium coordination between 6.5 and 7.5, consistent with experimental values for related crystalline phases [76]. A general decrease in coordination is observed with increasing oxygen substitution, reflecting the shorter Na–O bond length—about 0.5 Å less than Na–S—which constrains the expansion of the Na coordination shell. The difference between Na–S and Na–O distances is comparable across all simulations.

The magnitude of this decrease varies across the MLIPs: GRACE-GSE show the steepest drop, from ~7.4 to ~7.0; DeePMD shows a gentler decline, starting at ~7.1 and converging to similar final values. FT-MP0 predicts slightly lower values than GRACE-GSE (by 0.1–0.2) and exhibits an initial plateau or slight increase between x = 0 and x = 1. MATPES-based models and MP0 follow a similar trend, but with consistently lower coordination numbers (6.5–6.9 for the MATPESs and 6.3–6.6 for the MP). The differences in the coordination numbers predicted by the various MLIPs are most likely attributable to differences in their underlying training datasets and model architectures, while no correlation was found with Na-S and Na-O distances, as reported in Table S4 of the ESI. This interpretation is supported by the very similar coordination numbers obtained with the two MATPES-based potentials.

Across all MLIPs, sodium is found to coordinate preferentially with sulfur rather than oxygen. The fraction of Na–S decreases from 100 % in the pure sulfide glass to 63–68 % at x = 3.5 ($Na_4P_2S_{3.5}O_{3.5}$), while Na–O fraction increases correspondingly to 32–37 %. The persistence of Na–S preference, even at high oxygen substitution, highlights the stabilizing role of sulfur in the local sodium environment. This observation is consistent with the fact that the crossing point between BO and BS occurs before x = 3.5 and the one for NBO and NBS beyond x = 3.5, confirming that oxygen preferentially occupies bridging positions between phosphorus atoms rather than directly coordinating sodium.

4. Conclusions

In this study, we assessed six machine learning interatomic potentials for modelling $Na_4P_2S_{7-x}O_x$ glasses ($0 \leq x \leq 3.5$), a family of glassy solid electrolytes relevant for all-solid-state sodium batteries. These

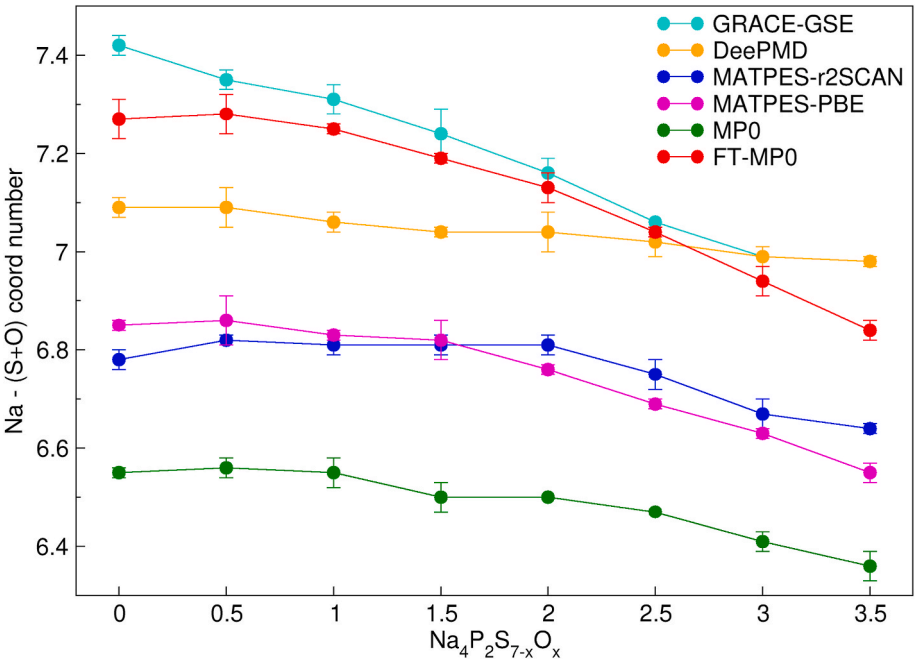

Fig. 9. Na – (S/O) coordination number of the $Na_4P_2S_{7-x}O_x$ GSEs simulated with the studied MLIPs.

compositions are structurally complex due to the non-linear evolution of density, conductivity and short-range order with oxygen content. Experimentally, oxygen incorporation drives a disproportionation reaction, converting P^1 units into P^0 and P^2, with oxygen preferentially occupying bridging sites.

The MLIPs tested include universal models (MP0. MATPES-PBE, MATPES-r2SCAN, GRACE-GSE), a system-specific DeePMD mode, and a fine-tuned variant (FT-MP0) MLIP derived from MP0. All of them demonstrated stable molecular dynamics behavior even when applied to systems substantially larger than those represented in their training datasets, like the one used here for the MD simulations.

While universal MLIPs provide stable MD trajectories and reasonable predictions of density and elastic properties, they often introduce structural artifacts such as edge-sharing units or P–P chains, and fail to reproduce the correct SRO evolution. DeePMD, trained via concurrent learning on crystalline structures shows similar limitations.

Among the UMLIPs, MATPES-based models -especially with r2SCAN perform better, highlighting the importance of diverse, high-quality datasets and functional choice. The fine-tuned FT-MP0 model, developed using composition-specific data, significantly improves structural accuracy, capturing density trends, mechanical properties, and oxygen's preference for bridging positions. However, it still struggles to reproduce the full disproportionation reaction.

These findings emphasize that while UMLIPs are useful starting points, fine-tuning is essential for accurate modeling of disordered systems. The training dataset must reflect not only the target composition but also the relevant structural motifs to ensure fidelity in both short- and medium-range order. Future work will expand the fine-tuning dataset to include more polymerized structures, explore MATPES-based models as starting points, and investigate the interplay between dispersion corrections and quench rate in shaping glass structure.

CRediT authorship contribution statement

Marco Bertani: Writing – original draft, Visualization, Validation, Methodology, Investigation, Formal analysis, Data curation, Conceptualization. **Alfonso Pedone:** Writing – review & editing, Supervision, Resources, Project administration, Funding acquisition, Conceptualization.

Declaration of competing interest

The authors declare no conflict of interest.

Acknowledgment

The University of Modena and Reggio Emilia is acknowledged for the financial support through the 'Finanziamento di Ateneo per la Ricerca' FAR2024 entitled 'Revolutionizing All-Solid-State Sodium Batteries with Advanced Computational Tools and Mixed Glass Former Effects', PI: Alfonso Pedone, CUP E93C24001990005. AP and MB acknowledge financial support from PNRR MUR project ECS_00000033_ECOSISTER. AP thanks NVIDIA for granting the project 'Neural Networks for Atomistic Simulations of Oxide Based Materials' through the donation of 1 NVIDIA A100 for PCIe within the NVIDIA Academic Hardware Grant Program. MB acknowledges ISCRA for awarding this project access to the LEONARDO supercomputer, owned by the EuroHPC Joint Undertaking, hosted by CINECA (Italy). Project name: AmElAiML. AP and MB acknowledge ICSC for awarding this project access to the LEONARDO supercomputer, owned by the EuroHPC Joint Undertaking, hosted by CINECA (Italy). Project name: CNHPC_1662286

Appendix A. Supplementary data

Supplementary data related to this article can be found online at https://doi.org/10.1016/j.solidstatesciences.2025.108204

Data availability

The training dataset and ASE and LAMMPS files for FT-MP0 MLIP are available at https://doi.org/10.5281/zenodo.18018824

References

[1] H. Bajolle, M. Lagadic, N. Louvet, The future of lithium-ion batteries: exploring expert conceptions, market trends, and price scenarios, Energy Res. Social Sci. 93 (2022) 102850, https://doi.org/10.1016/j.erss.2022.102850.
[2] J. Aylwin, M. Didier, O. Mora, The lithium industry and its human rights impacts: the case of the lickanantay people in Chile transboundary waters: the rio silala & the international court of justice: essays, Wyo Law Rev 23 (2) (2023) 107–114.

[3] H. Abelvik-Lawson, Indigenous Environmental Rights, Participation and Lithium Mining in Argentina and Bolivia: A Socio-Legal Analysis, University of Essex, 2019 phd.
[4] M.L. Vera, W.R. Torres, C.I. Galli, A. Chagnes, V. Flexer, Environmental impact of direct lithium extraction from brines, Nat. Rev. Earth Environ. 4 (3) (2023) 149–165, https://doi.org/10.1038/s43017-022-00387-5.
[5] D.B. Agusdinata, W. Liu, H. Eakin, H. Romero, Socio-environmental impacts of lithium mineral extraction: towards a research agenda, Environ. Res. Lett. 13 (12) (2018) 123001, https://doi.org/10.1088/1748-9326/aae9b1.
[6] C.S. Barrow, H. Lucia, M.F. Stock, Y. Alarie, Development of methodologies to assess the relative hazards from thermal decomposition products of polymeric materials, Am. Ind. Hyg. Assoc. J. 40 (5) (1979) 408–423, https://doi.org/10.1080/15298667991429769.
[7] S.C. Levy, Safety and reliability considerations for lithium batteries, J. Power Sources 68 (1) (1997) 75–77, https://doi.org/10.1016/S0378-7753(96)02622-5.
[8] J.W. Choi, D. Aurbach, Promise and reality of post-lithium-ion batteries with high energy densities, Nat. Rev. Mater. 1 (4) (2016) 1–16, https://doi.org/10.1038/natrevmats.2016.13.
[9] A. Manthiram, A reflection on lithium-ion battery cathode chemistry, Nat. Commun. 11 (1) (2020) 1550, https://doi.org/10.1038/s41467-020-15355-0.
[10] A.C. Radjendirane, D.K. Maurya, J. Ren, H. Hou, H. Algadi, B.B. Xu, et al., Overview of inorganic electrolytes for all-solid-state sodium batteries, Langmuir 40 (32) (2024) 16690–16712, https://doi.org/10.1021/acs.langmuir.4c01845.
[11] R. Borah, F.R. Hughson, J. Johnston, T. Nann, On battery materials and methods, Mater Today Adv 6 (2020) 100046, https://doi.org/10.1016/j.mtadv.2019.100046.
[12] F. Cheng, J. Liang, Z. Tao, J. Chen, Functional materials for rechargeable batteries, Adv. Mater. 23 (15) (2011) 1695–1715, https://doi.org/10.1002/adma.201003587.
[13] L. Porz, T. Swamy, B.W. Sheldon, D. Rettenwander, T. Frömling, H.L. Thaman, et al., Mechanism of lithium metal penetration through inorganic solid electrolytes, Adv. Energy Mater. 7 (20) (2017) 1701003, https://doi.org/10.1002/aenm.201701003.
[14] Y. Wang, S. Song, C. Xu, N. Hu, J. Molenda, L. Lu, Development of solid-state electrolytes for sodium-ion battery–A short review, Nano Mater. Sci. 1 (2) (2019) 91–100, https://doi.org/10.1016/j.nanoms.2019.02.007.
[15] X. Feng, P.-H. Chien, Z. Zhu, I.-H. Chu, P. Wang, M. Immediato-Scuotto, et al., Studies of functional defects for fast Na-ion conduction in Na3−yPS4−xClx with a combined experimental and computational approach, Adv. Funct. Mater. 29 (9) (2019) 1807951, https://doi.org/10.1002/adfm.201807951.
[16] F. Han, A.S. Westover, J. Yue, X. Fan, F. Wang, M. Chi, et al., High electronic conductivity as the origin of lithium dendrite formation within solid electrolytes, Nat. Energy 4 (3) (2019) 187–196, https://doi.org/10.1038/s41560-018-0312-z.
[17] W. Zhou, Y. Li, S. Xin, J.B. Goodenough, Rechargeable sodium all-solid-state battery, ACS Cent. Sci. 3 (1) (2017) 52–57, https://doi.org/10.1021/acscentsci.6b00321.
[18] Y. Seino, T. Ota, K. Takada, A. Hayashi, M. Tatsumisago, A sulphide lithium super ion conductor is superior to liquid ion conductors for use in rechargeable batteries, Energy Environ. Sci. 7 (2) (2014) 627–631, https://doi.org/10.1039/c3ee41655k.
[19] T. Minami, A. Hayashi, M. Tatsumisago, Recent progress of glass and glass-ceramics as solid electrolytes for lithium secondary batteries, Solid State Ionics 177 (26) (2006) 2715–2720, https://doi.org/10.1016/j.ssi.2006.07.017.
[20] J.H. Kennedy, Z. Zhang, H. Eckert, Ionically conductive sulfide-based lithium glasses, J. Non-Cryst. Solids 123 (1) (1990) 328–338, https://doi.org/10.1016/0022-3093(90)90804-U.
[21] W. Yao, S.W. Martin, Ionic conductivity of glasses in the MI + M2S + (0.1Ga2S3 + 0.9GeS2) system (M = Li, Na, K and Cs), Solid State Ionics 178 (33) (2008) 1777–1784, https://doi.org/10.1016/j.ssi.2007.10.011.
[22] M. Bertani, A. Pedone, Atomic structure of Na4P2S7 glass solid electrolyte: fine-tuning machine learning potentials for enhanced accuracy, J. Phys. Chem. C 129 (28) (2025) 12697–12709, https://doi.org/10.1021/acs.jpcc.5c01857.
[23] S. Kmiec, A. Joyce, S.W. Martin, Glass formation and structural analysis of Na4P2S7-xOx, $0 \leq x \leq 7$ sodium oxy-thiophosphate glasses, J. Non-Cryst. Solids 498 (2018) 177–189, https://doi.org/10.1016/j.jnoncrysol.2018.06.007.
[24] M. Lazar, S. Kmiec, A. Joyce, S.W. Martin, Investigations into reactions between sodium metal and Na3PS4–xOx solid-state electrolytes: enhanced stability of the Na3PS3O solid-state electrolyte, ACS Appl. Energy Mater. 3 (12) (2020) 11559–11569, https://doi.org/10.1021/acsaem.0c00914.
[25] K. Luo, R. Zhou, S.W. Martin, Q. An, Flexible doorway controlled Na+ ion diffusion in NaPSO glassy electrolytes from machine-learning force field simulations, J. Mater. Chem. A 12 (48) (2024) 33518–33525, https://doi.org/10.1039/D4TA05071A.
[26] S. Kmiec, M. Olson, M. Kenney, S.W. Martin, Interpretation of the Na+ ionic conductivity in Na4P2S7–xOx mixed oxy-sulfide glasses: effects of oxygen doping, Chem. Mater. 34 (21) (2022) 9479–9491, https://doi.org/10.1021/acs.chemmater.2c01934.
[27] A. Joyce, S. Kmiec, S.W. Martin, Glass transition temperature studies of planetary ball milled glasses: accessing the rapidly cooled glassy state in Na4P2S7-xOx, $0 \leq x \leq 7$, Oxy-thio phosphate glasses, J. Non-Cryst. Solids 551 (2021) 120462, https://doi.org/10.1016/j.jnoncrysol.2020.120462.
[28] S. Urata, M. Bertani, A. Pedone, Applications of machine-learning interatomic potentials for modeling ceramics, glass, and electrolytes: a review, J. Am. Ceram. Soc. 107 (12) (2024) 7665–7691, https://doi.org/10.1111/jace.19934.
[29] M. Bertani, T. Charpentier, F. Faglioni, A. Pedone, Accurate and transferable machine learning potential for molecular dynamics simulation of sodium silicate glasses, J. Chem. Theor. Comput. (2024), https://doi.org/10.1021/acs.jctc.3c01115.
[30] S. Urata, Modeling short-range and three-membered ring structures in lithium borosilicate glasses using a machine-learning potential, J. Phys. Chem. C 126 (50) (2022) 21507–21517, https://doi.org/10.1021/acs.jpcc.2c07597.
[31] S. Urata, N. Nakamura, T. Tada, A.R. Tan, R. Gómez-Bombarelli, H. Hosono, Suppression of Rayleigh scattering in silica glass by codoping boron and fluorine: molecular dynamics simulations with force-matching and neural network potentials, J. Phys. Chem. C 126 (4) (2022) 2264–2275, https://doi.org/10.1021/acs.jpcc.1c10300.
[32] S. Ju, J. You, G. Kim, Y. Park, H. An, S. Han, Application of pretrained universal machine-learning interatomic potential for physicochemical simulation of liquid electrolytes in Li-ion battery. https://doi.org/10.48550/arXiv.2501.05211, 2025.
[33] B. Deng, P. Zhong, K. Jun, J. Riebesell, K. Han, C.J. Bartel, et al., CHGNet as a pretrained universal neural network potential for charge-informed atomistic modelling, Nat. Mach. Intell. 5 (9) (2023) 1031–1041, https://doi.org/10.1038/s42256-023-00716-3.
[34] I. Batatia, P. Benner, Y. Chiang, A.M. Elena, D.P. Kovács, J. Riebesell, et al., A foundation model for atomistic materials chemistry. https://doi.org/10.48550/arXiv.2401.00096, 2024.
[35] Foundation Models - Gracemaker. n.d.
[36] C. Chen, S.P. Ong, A universal graph deep learning interatomic potential for the periodic table, Nat. Comput. Sci. 2 (11) (2022) 718–728, https://doi.org/10.1038/s43588-022-00349-3.
[37] H. Yang, C. Hu, Y. Zhou, X. Liu, Y. Shi, J. Li, et al., MatterSim: A Deep Learning Atomistic Model across Elements, Temperatures and Pressures, 2024, https://doi.org/10.48550/arXiv.2405.04967.
[38] M. Neumann, J. Gin, B. Rhodes, S. Bennett, Z. Li, H. Choubisa, et al., Orb: a fast, Scalable Neural Network Potential (2024), https://doi.org/10.48550/arXiv.2410.22570.
[39] A. Pedone, M. Bertani, M. Benassi, Revisiting machine learning potentials for silicate glasses: the missing role of dispersion interactions, J. Chem. Theor. Comput. 21 (9) (2025) 4769–4778, https://doi.org/10.1021/acs.jctc.5c00218.
[40] S. Mannan, V. Bihani, C. Gonzales, K.L.K. Lee, N.N. Gosvami, S. Ranu, et al., Evaluating universal machine learning force fields against experimental measurements. https://doi.org/10.48550/arXiv.2508.05762, 2025.
[41] A. Jain, S.P. Ong, G. Hautier, W. Chen, W.D. Richards, S. Dacek, et al., Commentary: the Materials Project: a materials genome approach to accelerating materials innovation, APL Mater. 1 (1) (2013) 011002, https://doi.org/10.1063/1.4812323.
[42] M.K. Horton, P. Huck, R.X. Yang, J.M. Munro, S. Dwaraknath, A.M. Ganose, et al., Accelerated data-driven materials science with the Materials Project, Nat. Mater. 24 (10) (2025) 1522–1532, https://doi.org/10.1038/s41563-025-02272-0.
[43] A.D. Kaplan, R. Liu, J. Qi, T.W. Ko, B. Deng, J. Riebesell, et al., A foundational potential energy surface dataset for materials. https://doi.org/10.48550/arXiv.2503.04070, 2025.
[44] J.P. Perdew, K. Burke, M. Ernzerhof, Generalized gradient approximation made simple, Phys. Rev. Lett. 77 (18) (1996) 3865–3868, https://doi.org/10.1103/PhysRevLett.77.3865.
[45] J.W. Furness, A.D. Kaplan, J. Ning, J.P. Perdew, J. Sun, Accurate and numerically efficient r2SCAN meta-generalized gradient approximation, J. Phys. Chem. Lett. 11 (19) (2020) 8208–8215, https://doi.org/10.1021/acs.jpclett.0c02405.
[46] J. Behler, M. Parrinello, Generalized neural-network representation of high-dimensional potential-energy surfaces, Phys. Rev. Lett. 98 (14) (2007) 146401, https://doi.org/10.1103/PhysRevLett.98.146401.
[47] A.P. Bartók, R. Kondor, G. Csányi, On representing chemical environments, Phys. Rev. B 87 (18) (2013) 184115, https://doi.org/10.1103/PhysRevB.87.184115.
[48] I. Batatia, D.P. Kovács, G.N.C. Simm, C. Ortner, G. Csányi, MACE: higher order equivariant message passing neural networks for fast and accurate force fields. https://doi.org/10.48550/arXiv.2206.07697, 2023.
[49] ACEsuit/Mace-Foundations, 2025.
[50] R. Christensen, M.M. Smedskjaer, Accelerating the discovery of high-conductivity glass electrolytes via machine learning. https://doi.org/10.26434/chemrxiv-2025-7csf2, 2025.
[51] L. Barroso-Luque, M. Shuaibi, X. Fu, B.M. Wood, M. Dzamba, M. Gao, et al., Open materials 2024 (OMat24) inorganic materials dataset and models. https://doi.org/10.48550/arXiv.2410.12771, 2024.
[52] A. Bochkarev, Y. Lysogorskiy, R. Drautz, Graph atomic cluster expansion for semilocal interactions beyond equivariant message passing, Phys. Rev. X 14 (2) (2024) 021036, https://doi.org/10.1103/PhysRevX.14.021036.
[53] M.W. Finnis, J.E. Sinclair, A simple empirical N-body potential for transition metals, Philos. Mag. A 50 (1) (1984) 45–55, https://doi.org/10.1080/01418618408244210.
[54] Y. Zhang, H. Wang, W. Chen, J. Zeng, L. Zhang, H. Wang, et al., DP-GEN: a concurrent learning platform for the generation of reliable deep learning based potential energy models, Comput. Phys. Commun. 253 (2020) 107206, https://doi.org/10.1016/j.cpc.2020.107206.
[55] J. Zeng, D. Zhang, D. Lu, P. Mo, Z. Li, Y. Chen, et al., DeePMD-kit v2: a software package for Deep Potential models. https://doi.org/10.48550/arXiv.2304.09409, 2023.
[56] Multihead Replay Finetuning — Mace 0.3.13 Documentation. n.d.
[57] A. Pedone, G. Malavasi, M.C. Menziani, U. Segre, A.N. Cormack, Molecular dynamics studies of Stress−Strain behavior of silica glass under a tensile load, Chem. Mater. 20 (13) (2008) 4356–4366, https://doi.org/10.1021/cm800413v.

[58] J. Hutter, M. Iannuzzi, F. Schiffmann, J. VandeVondele, cp2k: atomistic simulations of condensed matter systems, WIREs Comput Mol Sci 4 (1) (2014) 15–25, https://doi.org/10.1002/wcms.1159.
[59] S.P. Niblett, P. Kourtis, I.-B. Magdău, C.P. Grey, G. Csányi, Transferability of datasets between machine-learning interaction potentials. https://doi.org/10.48550/arXiv.2409.05590, 2024.
[60] A.P. Thompson, H.M. Aktulga, R. Berger, D.S. Bolintineanu, W.M. Brown, P. S. Crozier, et al., LAMMPS - a flexible simulation tool for particle-based materials modeling at the atomic, meso, and continuum scales, Comput. Phys. Commun. 271 (2022) 108171, https://doi.org/10.1016/j.cpc.2021.108171.
[61] S. Nose, Constant-temperature molecular dynamics, J. Phys. Condens. Matter 2 (S) (1990) SA115–SA119, https://doi.org/10.1088/0953-8984/2/S/013.
[62] A. Pedone, G. Malavasi, A.N. Cormack, U. Segre, M.C. Menziani, Insight into elastic properties of binary alkali silicate glasses; prediction and interpretation through atomistic simulation techniques, Chem. Mater. 19 (13) (2007) 3144–3154, https://doi.org/10.1021/cm062619r.
[63] M. Bertani, M.C. Menziani, A. Pedone, Improved empirical force field for multicomponent oxide glasses and crystals, Phys. Rev. Mater. 5 (4) (2021) 045602, https://doi.org/10.1103/PhysRevMaterials.5.045602.
[64] T. Tan, S. Yin, K. Liu, M. Wan, On the convergence speed of AMSGRAD and beyond, in: 2019 IEEE 31st Int. Conf. Tools Artif. Intell. ICTAI, 2019, pp. 464–470, https://doi.org/10.1109/ICTAI.2019.00071.
[65] E. Martin, I.B.A. Essomba, K. Ishisone, M. Boero, G. Ori, C. Massobrio, et al., Impact of dispersion force schemes on liquid systems: comparing efficiency and drawbacks for well-targeted test cases, Molecules 27 (24) (2022), https://doi.org/10.3390/molecules27249034.
[66] S. Nishimura, N. Tanibata, A. Hayashi, M. Tatsumisago, A. Yamada, The crystal structure and sodium disorder of high-temperature polymorph β-Na3PS4, J. Mater. Chem. A 5 (47) (2017) 25025–25030, https://doi.org/10.1039/C7TA08391B.
[67] M. Pompetzki, M. Jansen, Natriumtrithiophosphat(V): Kristallstruktur und Natriumionenleitfähigkeit, Z. Anorg. Allg. Chem. 629 (11) (2003) 1929–1933, https://doi.org/10.1002/zaac.200300170.
[68] K.Y. Leung, C. Calvo, The structure of Na4P2O7 at 22 °C, Can. J. Chem. 50 (16) (1972) 2519–2526, https://doi.org/10.1139/v72-406.
[69] R. Kingsbury, A.S. Gupta, C.J. Bartel, J.M. Munro, S. Dwaraknath, M. Horton, et al., Performance comparison of ${r}^{2}\mathrm{SCAN}$ and SCAN metaGGA density functionals for solid materials via an automated, high-throughput computational workflow, Phys. Rev. Mater. 6 (1) (2022) 013801, https://doi.org/10.1103/PhysRevMaterials.6.013801.
[70] M. Kothakonda, A.D. Kaplan, E.B. Isaacs, C.J. Bartel, J.W. Furness, J. Ning, et al., Testing the r2SCAN Density Functional for the Thermodynamic Stability of Solids with and without a van der Waals Correction, ACS Mater. Au 3 (2) (2023) 102–111, https://doi.org/10.1021/acsmaterialsau.2c00059.
[71] E. Caldeweyher, J.-M. Mewes, S. Ehlert, S. Grimme, Extension and evaluation of the D4 London-dispersion model for periodic systems, Phys. Chem. Chem. Phys. 22 (16) (2020) 8499–8512, https://doi.org/10.1039/D0CP00502A.
[72] M. Kothakonda, A.D. Kaplan, E.B. Isaacs, C.J. Bartel, J.W. Furness, J. Ning, et al., Testing the r2SCAN Density Functional for the Thermodynamic Stability of Solids with and without a van der Waals Correction, ACS Mater. Au 3 (2) (2023) 102–111, https://doi.org/10.1021/acsmaterialsau.2c00059.
[73] C. Calahoo, L. Wondraczek, Ionic glasses: structure, properties and classification, J. Non-Cryst. Solids X 8 (2020) 100054, https://doi.org/10.1016/j.nocx.2020.100054.
[74] C. Dietrich, D.A. Weber, S.J. Sedlmaier, S. Indris, S.P. Culver, D. Walter, et al., Lithium ion conductivity in Li2S–P2S5 glasses – building units and local structure evolution during the crystallization of superionic conductors Li3PS4, Li7P3S11 and Li4P2S7, J. Mater. Chem. A 5 (34) (2017) 18111–18119, https://doi.org/10.1039/C7TA06067J.
[75] A. Dive, Y. Zhang, Y. Yao, S.W. Martin, S. Banerjee, Investigations of the structure of Na2S + P2S5 glassy electrolytes and its impact on Na+ ionic conductivity through *ab initio* molecular dynamics, Solid State Ionics 338 (2019) 177–184, https://doi.org/10.1016/j.ssi.2019.05.014.
[76] M. Jansen, U. Henseler, Synthesis, structure determination, and ionic conductivity of sodium tetrathiophosphate, J. Solid State Chem. 99 (1) (1992) 110–119, https://doi.org/10.1016/0022-4596(92)90295-7.